

## DSC solution for flow in a staggered double lid driven cavity

Y. C. Zhou<sup>1</sup>, B. S. V. Patnaik<sup>2</sup>, D. C. Wan<sup>2,†</sup> and G. W. Wei<sup>1,2,\*,‡</sup>

<sup>1</sup>*Department of Mathematics, Michigan State University, East Lansing, MI 48824, U.S.A.*

<sup>2</sup>*Department of Computational Science, National University of Singapore, Singapore 117543*

### SUMMARY

A benchmark quality solution is presented for flow in a staggered double lid driven cavity obtained by using the wavelet-based discrete singular convolution (DSC). The proposed wavelet based algorithm combines local methods' flexibility and global methods' accuracy, and hence, is a promising approach for achieving the high accuracy solution of the Navier–Stokes equations. Block structured grids with pseudo-overlapping subdomains are employed in the present simulation. A third order Runge–Kutta scheme is used for the temporal discretization. Quantitative results are presented, apart from the qualitative fluid flow patterns. The prevalence of rich features of flow morphology, such as two primary vortex patterns, merged single primary vortex patterns, and secondary eddies, makes this problem very attractive and interesting. The problem is quite challenging for the possible existence of numerically induced asymmetric flow patterns and elliptic instability. Important computational issues like consistence, convergence and reliability of the numerical scheme are examined. The DSC algorithm is tested on the single lid driven cavity flow and the Taylor problem with a closed form solution. The double lid driven cavity simulations are cross-validated with the standard second order finite volume method. Copyright © 2003 John Wiley & Sons, Ltd.

KEY WORDS: benchmark solution; CFD; cavity flows; wavelets; discrete singular convolution

### 1. INTRODUCTION

Owing to a continuous increase in computing power and the improvement in numerical algorithms, computation is now regarded as an indispensable and equally powerful approach, along with theory and experiment, in the study of fluid dynamics. Computation enables the study of complex systems and natural phenomena that would be too expensive, dangerous, or even impossible, to investigate by direct experimentation in a laboratory. The desire for better

---

\*Correspondence to: G. W. Wei, Department of Mathematics, Michigan State University, East Lansing, MI 48824, U.S.A.

†Current address: Institute for Applied Mathematics, University of Dortmund, Germany.

‡E-mail: wei@math.msu.edu

Contract/grant sponsor: National University of Singapore

Contract/grant sponsor: National Science and Technology Board

*Received 30 August 2001*

*Revised 8 May 2002*

*Accepted 12 July 2002*

understanding of turbulent flow, multiphase flow, flow in complex geometry, fluid–structure interaction, etc. provide great impetus to the development of new computer architecture and better computational algorithms. The latter involves several important issues like, accuracy, consistence, stability, and reliability, whose validation has become both inevitable and crucial to the improvement and recognition of new computational schemes. Such validation in turn necessitates a common platform for the examination of potential computational schemes and algorithms. To this end, several benchmark problems have become popular in the open literature, e.g. the (single) lid driven cavity, flow over backward facing step, buoyancy driven cavity, flow past a circular cylinder, flow past a square cylinder, etc. Although there is a vast amount of literature, the quest for an ideal test problem still continues. Further, all these existing benchmark problems come under the category of well understood problems. Therefore, it is natural that the CFD community continuously embraces new benchmark problems, which possess the properties of both computational complexity and richness in physics. To this end, it is desirable to look at the basic attributes of a benchmark problem. In our view, the geometry of a fluid flow domain should preferably, be simple but not trivial. The boundary conditions should be very well defined and with complete lack of ambiguity. An additional requirement which can really spur motivation is the presence of rich and complex fluid flow patterns. The availability of theoretical and/or experimental data for the purpose of comparison will have an additional advantage. Then, the real concern for the numerical scheme would be the accuracy and stability with which these patterns can be simulated by the scheme. It is in this context that in a recent review, Shankar and Deshpande [1] have pointed out that, driven cavity flows exhibit almost all the phenomena that can possibly occur in incompressible flows: eddies, secondary flows, complex three-dimensional patterns, chaotic particle motions, instability, and turbulence. Thus, these broad spectra of features make the cavity flows overwhelmingly attractive for examining the computational schemes. However, some other interesting flow phenomena, such as elliptical instability, cannot occur in this model. Elliptical instability and solution multiplicity have been recently reported in a double shear driven cavity [2]. In such investigation, fluid flow stability has been studied by both experimental and numerical means [3]. However, the geometry of both the single lid driven cavity and double lid driven cavity is in fact too simple, from the numerical view point. Therefore, additional constraints have to be imposed for validating a numerical scheme for complex geometries.

In compliance with the above views, the problem of staggered double lid driven cavity is considered. Although at the very outset, the geometry looks like a simple extension of the double lid driven cavity, it is a much more complex problem. The domain of the staggered double lid driven cavity has all the essential features of a complex cavity and in some sense, looks like a synthesis of two popular benchmark problems viz. a lid driven cavity and a backward facing step. This problem was earlier introduced by Hinatsu and Ferziger [4]. However, to the best of our knowledge, no quantitative results have been reported in the literature. Numerically, the staggered double shear driven cavity is a nontrivial extension of a lid driven cavity. It poses three additional difficulties. First, the geometry of the problem is no longer a simple square box. Therefore, different approaches, such as, domain decomposition, can be introduced to account for the geometric complexity. Secondly, the inherent symmetry of the problem requires a symmetric representation in the flow pattern for certain range of Reynold's numbers, which imposes a severe challenge to the computational scheme in terms of numerical accuracy and reliability. A small perturbation can be amplified in the long time integration

and can lead to an asymmetric flow pattern. Finally, the possible presence of elliptic instability in this system poses another hurdle for its numerical simulation. However, the occurrence of solution multiplicity has to be verified carefully against the possibility of numerically induced asymmetric patterns. Therefore, a reliable numerical scheme is indispensable for the present study.

The large variety of available numerical schemes can be classified under two categories viz. global and local methods. Global methods, such as spectral methods [5, 6], pseudospectral methods [7], fast Fourier transform [8, 9], differential quadrature [10], approximate a differentiation at a point by all the grid points in the computational domain, and thus can be highly accurate. For example, spectral methods converge exponentially with respect to mesh refinement for approximating an analytic function [7] and thus, has the potential for being used in high precision computations. Several global methods have been successfully used for the simulation of both internal and external flows. However, global methods are well known for their limitations in handling complex geometries and boundary conditions. Indeed, for engineering fluid flow simulations, finite differences [11, 12], finite elements [13–16], finite strips [17], and finite volumes [18], are the dominant approaches. Local methods utilize information at the nearest neighbouring grid points to approximate a differentiation at a point and thus, are much more flexible in handling irregular geometries. However, local methods have disadvantages, such as slower convergence with respect to mesh refinement and thus, are very expensive to achieve a high accuracy computation. There are two ways to extend the applicability of global methods to complex domains. One approach is to divide the computational domain into a number of regular subdomains. within which spectral methods are implemented to achieve high accuracy [19, 20]. The second approach involves mapping of an irregular computational domain into a regular one, in which spectral methods can be implemented.

Recently, the discrete singular convolution (DSC) algorithm was proposed as a potential approach for the computer realization of singular integrations [21–23]. The theory of distribution and wavelet analysis forms the mathematical foundation for the DSC. Sequences of approximations to the singular kernels of Hilbert, Abel and delta types were constructed. Applications to analytical signal processing, Radon transform and surface interpolation are discussed. Numerical solutions to differential equations are formulated via singular kernels of the delta type. By appropriately choosing the DSC kernels, the DSC approach exhibits global methods' accuracy for integration and local methods' flexibility in handling complex geometries and boundary conditions. Many DSC kernels, such as (regularized) Shannon's delta kernel, (regularized) Dirichlet kernel, (regularized) Lagrange kernel and (regularized) de la Vallée Poussin kernels, are constructed for a number of applications, such as numerical solutions of the Fokker–Planck equation [21, 22] and the Schrödinger equation [24]. The DSC algorithm was also used for waveguide model analysis, electromagnetic wave propagation [25] and structural (plate and beam) analysis [26–28] with excellent results. It was used to facilitate a new synchronization scheme for shock capturing [29]. Most recently, the DSC algorithm was used to resolve a few numerically challenging problems. It was utilized to integrate the (non-linear) sine-Gordon equation with the initial values close to a homoclinic orbit singularity [30], for which conventional local methods encounter great difficulties and numerically induced chaos was reported [31]. Another difficult example resolved by using the DSC algorithm is the integration of the (nonlinear) Cahn–Hilliard equation in a circular domain, which is challenging because of the fourth order artificial singularity at the origin and the complex phase space geometry [32]. Analyses of plates vibrating at extremely

high frequency and with densely distributed internal supports are very challenging tasks. Conventional methods have encountered great difficulty of numerical instability for such analyses. The DSC algorithm found its success in resolving these problems [33, 34]. The DSC solution of the Navier–Stokes equations is of primary interest to the present study. The standard Taylor problem was solved to machine precision with just 33 grid points in each dimension [26]. A DSC-successive over relaxation (DSC-SOR) algorithm was developed for simulating the incompressible viscous flows [35, 36]. The objective of the present work is to explore the flow phenomena in the staggered double lid driven cavity and to present benchmark quality solution for this problem. Numerical issues such as consistence, convergence, stability and reliability are addressed. Some of the DSC results are cross-validated by using a completely different numerical scheme, a standard second order finite volume approach. It is believed that interesting flow features observed in the present investigation will be useful for validating emerging computational schemes and for possible experimental studies on this geometry.

The subsequent sections are organized as follows: Theoretical formulation is presented in Section 2 to describe the problem and the DSC algorithm. Section 3 is devoted to the solution scheme. Results of the numerical simulations are presented in Section 4. In this section, both qualitative fluid flow patterns and quantitative results are presented, apart from consistence and convergence issues. The paper ends with a conclusion.

## 2. THEORETICAL FORMULATION

This section describes the problem and its governing partial differential equations. The philosophy behind the discrete singular convolution is briefly discussed.

### 2.1. The mathematical model

A staggered double shear driven cavity can be thought of as two superimposed square cavities diagonally offset by 40%. Both the upper and lower cavities are staggeredly combined and have a unified boundary. For the sake of convenience, all the corners are labelled as in Figure 1. The lid (DE) on the upper cavity is a wall which continuously moves towards the right, and the lid (AH) on the lower cavity moves towards the left as shown in Figure 1. The fluid flow features inside the cavity described above, can be simulated by a set of mass and momentum conservation equations. The flow is assumed to be two-dimensional, laminar, incompressible and Newtonian. The governing non-linear partial differential equations can be written as follows:

continuity equation:

$$\frac{\partial u}{\partial x} + \frac{\partial v}{\partial y} = 0 \quad (1)$$

*x*-momentum equation:

$$\frac{\partial u}{\partial t} + u \frac{\partial u}{\partial x} + v \frac{\partial u}{\partial y} = -\frac{\partial p}{\partial x} + \frac{1}{Re} \left( \frac{\partial^2 u}{\partial x^2} + \frac{\partial^2 u}{\partial y^2} \right) \quad (2)$$

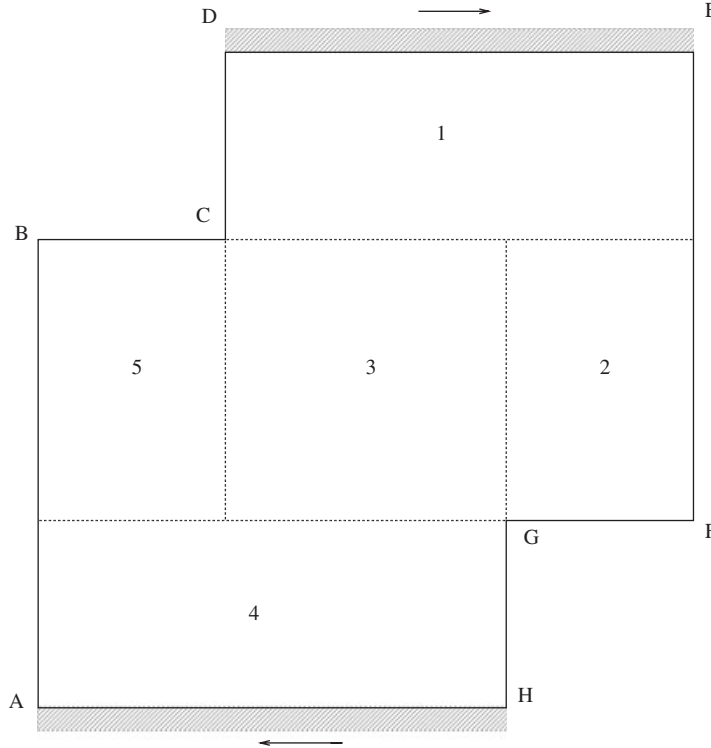


Figure 1. The configuration of staggered double lid driven cavity with pseudodomain demarcation.

y-momentum equation:

$$\frac{\partial v}{\partial t} + u \frac{\partial v}{\partial x} + v \frac{\partial v}{\partial y} = -\frac{\partial p}{\partial y} + \frac{1}{Re} \left( \frac{\partial^2 v}{\partial x^2} + \frac{\partial^2 v}{\partial y^2} \right) \quad (3)$$

The above equations were non-dimensionalized as follows:

$$x = \frac{\bar{x}}{L_{ref}}; \quad y = \frac{\bar{y}}{L_{ref}}; \quad u = \frac{\bar{u}}{U_{ref}}; \quad v = \frac{\bar{v}}{U_{ref}} \quad (4)$$

and

$$t = \frac{\bar{t} U_{ref}}{L_{ref}}; \quad p = \frac{\bar{p}}{\rho U_{ref}^2}; \quad Re = \frac{U_{ref} L_{ref}}{\nu} \quad (5)$$

In these equations, the values with an over bar refer to the corresponding dimensional variables. The  $L_{ref}$  is the reference length dimension (width of the cavity along the upper or lower lid), while  $U_{ref}$  is the reference velocity dimension. The fluid property  $\nu$ , refers to the kinematic viscosity. The Reynold's number,  $Re$ , is the ratio of inertial to viscous forces, which influences the fluid flow features within the cavity.

*2.1.1. Boundary conditions.* No-slip velocity boundary condition ( $u=v=0.0$ ) is applied on all the walls, except the top and bottom lids. On the top lid ( $u=1.0$ ;  $v=0.0$ ) is applied, while on the bottom lid ( $u=-1.0$ ;  $v=0.0$ ) is enforced as a part of the moving wall boundary condition.

For the convenience of presenting the method of solution, we define

$$D(U) = \frac{\partial u}{\partial x} + \frac{\partial v}{\partial y} \quad (6)$$

$$L(U) = F(U) - \nabla p \quad (7)$$

$$F(U) = [f, g]^T, \quad U = [u, v]^T, \quad \nabla p = \left[ \frac{\partial p}{\partial x}, \frac{\partial p}{\partial y} \right]^T \quad (8)$$

$$f = \frac{1}{Re} \left( \frac{\partial^2 u}{\partial x^2} + \frac{\partial^2 u}{\partial y^2} \right) - \left( u \frac{\partial u}{\partial x} + v \frac{\partial u}{\partial y} \right), \quad g = \frac{1}{Re} \left( \frac{\partial^2 v}{\partial x^2} + \frac{\partial^2 v}{\partial y^2} \right) - \left( u \frac{\partial v}{\partial x} + v \frac{\partial v}{\partial y} \right) \quad (9)$$

Therefore, the system of equations (1)–(3) can be simplified as

$$D(U) = 0 \quad (10)$$

$$\frac{\partial U}{\partial t} = L(U) = F(U) - \nabla p \quad (11)$$

These governing equations are used for flow simulations in complex geometries. Their spatial and temporal discretizations are described in the rest of this section.

## 2.2. Discrete singular convolution

Singular convolutions (SC) are a special class of mathematical transformations, which appear in many science and engineering problems, such as Hilbert transform, Abel transform and Radon transform. It is most convenient to discuss the singular convolution in the context of the theory of distributions. The latter has a significant impact in mathematical analysis. Discrete singular convolution provides a numerical realization of the singular convolution. In this part, we will present the formulation of DSC in approximation of the spatial derivatives. We recommend References [21–23] for its mathematical details.

A typical DSC approximation to  $q$ th order derivative of a function  $f(x)$ , which is only available at a set of discrete values  $f(x_k)$ , can be given by

$$f^{(q)}(x) \approx \sum_{k=-W}^W \delta_{\sigma, \Delta}^{(q)}(x - x_k) f(x_k), \quad q = 0, 1, 2, \dots \quad (12)$$

where  $\delta_{\sigma, \Delta}(x - x_k)$  is a DSC kernel. There are a variety of different DSC kernels that could be used for the present work. A frequently used DSC kernel is the regularized Shannon kernel (RSK)

$$\delta_{\sigma, \Delta}(x - x_k) = \frac{\sin \pi/\Delta(x - x_k)}{\pi/\Delta(x - x_k)} \exp \left( -\frac{(x - x_k)^2}{2\sigma^2} \right) \quad (13)$$

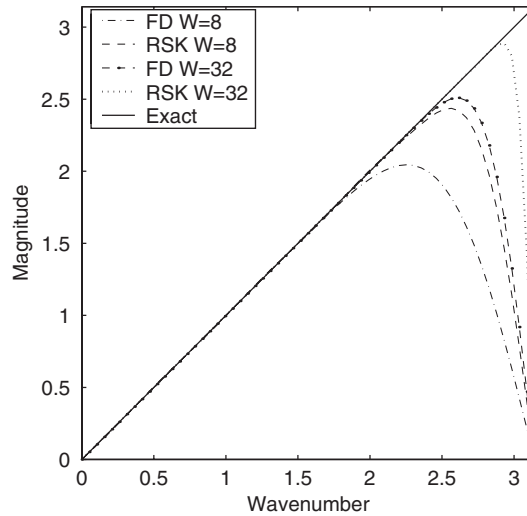


Figure 2. Comparison of dispersion relations of the finite difference (FD) scheme and regularized Shannon kernel (RSK).

where  $\sigma$  controls the width of the Gaussian window. In numerical computation, an optimal result can be attained if this window is related to the grid spacing  $\Delta$  by  $r = \sigma/\Delta$ , which in turn depends on the computational support  $W$ . High accuracy approximations can be obtained by choosing appropriate combinations of  $W$  and  $r$ . Some commonly used pairs are  $W=8$ ,  $r=2.0$ ;  $W=16$ ,  $r=2.6$  and  $W=32$ ,  $r=3.5$ . It may be noted that the DSC algorithm actually provides a systemic procedure to generate high order finite difference schemes [22], i.e. difference coefficients for high order derivatives can be generated by differentiating the kernel  $\delta_{\sigma,\Delta}(x - x_k)$ . By taking the advantage of varying  $W$ , DSC scheme can be customized to obtain desired accuracy for a given task. Moreover, for a given  $W$ , the DSC algorithm can be more accurate than the standard finite difference scheme as shown in Figure 2, in which approximations to the first order derivative are compared. Mathematical analysis [37] indicates that the approximation error of the RSK for certain bandlimited functions decays exponentially as  $W$  increases, which confirms the spectral feature of the DSC algorithm.

### 3. SOLUTION SCHEME

One of the major difficulties in numerically solving incompressible Navier–Stokes equations is the lack of an explicit evolution equation for pressure. Generally, there are two issues associated with this problem: how to ‘derive’ a governing equation for pressure and how to propose appropriate boundary conditions for this additional equation, if necessary. For this purpose, many specially designed schemes have been developed in the literature [18, 38]. In the present investigation, we adopt a fractional-time-step and potential-function method (FTSPFM) [35, 36], which is a variant of the MAC method for solving the governing Equations (10) and (11).

The DSC algorithm deals with the boundary conditions by using a ‘ghost-point’ approach. For no-slip boundary conditions of the velocity, the values at ‘ghost-points’ are set to the velocity of the solid boundary. The governing equation introduced for pressure, i.e. the potential function, admits homogeneous boundary condition. Thus, its values outside the computational domain are obtained by the symmetric extension. Validation by using the analytically solvable Taylor problem and a comparison with the benchmark solution on the single lid-driven cavity verify that the present treatment is feasible to general boundary conditions for flow problems.

### 3.1. Pseudo-overlapping block-structured grid

In this subsection, domain decomposition, spatial and temporal discretization are described. Multiblock grids are considerably more flexible in handling complex geometries than single-block grids. Typically, block-structured grids of matched interfaces, non-matching interfaces and overlapped interfaces are used for decomposing complex and irregular geometries. In the present method, the computational domain is first divided into a number of simple rectangular blocks (or subdomains). Two neighbouring blocks are joined together along a common grid line. Different subdomains may have very different geometric sizes and mesh sizes (i.e. non-matching interfaces). Therefore, one can reduce the topological complexity of an irregular computational domain by employing several simple regular subdomains. Moreover, it permits the grid of each individual subdomain to be generated independently, so that, both geometry and resolution in the boundary region can be treated in a desired manner. In the present study, we divide the total computational domain of the staggered double lid driven cavity into five subdomains as illustrated in Figure 1.

The present treatment of block interfaces is different from the conventional approaches, due to the existence of pseudodomains. As discussed earlier, the DSC algorithm requires pseudodomains at computational boundaries. Such a pseudodomain of one subdomain may overlap with the computational domain of a neighbouring subdomain. This relation is illustrated in Figure 3(a). Block ABDC, shown in Figure 3(a), is the original computational domain, and is split into two subdomains ABFE and EFDC, as shown in Figure 3(a). The dashed line EF is the common line connecting block ABFE and block EFDC. The area of GHFE is a pseudodomain of EFDC and a *pseudo-overlapping zone* for subdomain ABFE. Similarly, the area of EFJI is a pseudodomain of ABFE and a *pseudo-overlapping zone* for subdomain EFDC. The size of pseudo-overlapping zones is determined by the computational bandwidth  $W$  chosen in the DSC algorithm. Hence, it is very flexible to adjust the size of the overlapping zones to meet the accuracy requirement of different problems by changing the value of the computational bandwidth  $W$ .

It is important to note that, the requirement of mutual positioning or communication between adjacent blocks can have a considerable influence on the efficiency of numerical calculations. If the grid size used in every subdomain is the same (i.e. matched interfaces), then information exchange between adjacent blocks is simple: one just needs to assign nodal values directly at the pseudo-overlapping zone of one subdomain to those at the pseudodomain of its adjacent subdomain. If different grids are employed in two neighbouring subdomains (non-matching interfaces), pseudo-overlapping zone will have two different grids. In such a case, a special treatment is required to transfer information from the pseudo-overlapping zone of one subdomain to the pseudodomain of its adjacent subdomain. In the present approach, such an information exchange is realized by using the DSC interpolation algorithm. Specifically,

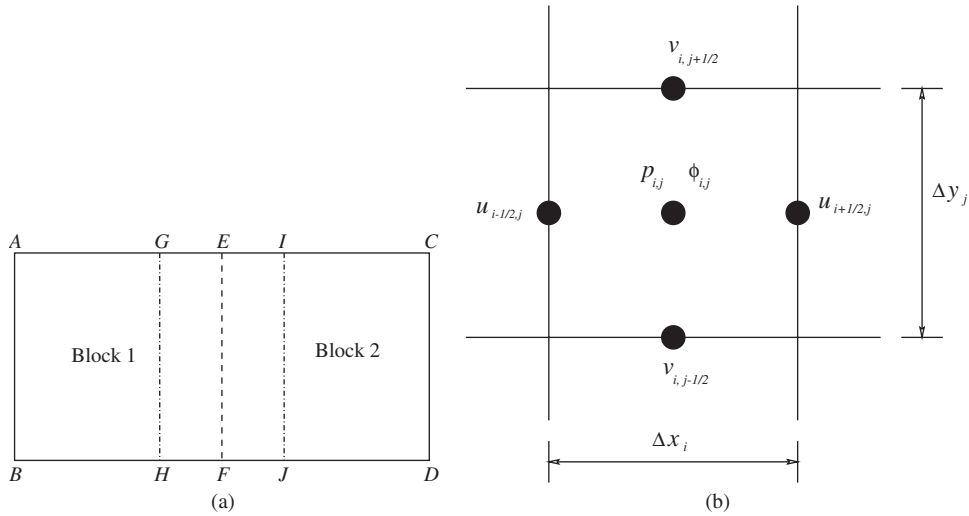


Figure 3. (a) Subdomain division with interfaces and pseudo-overlapping zones; and (b) the staggered grid system.

the DSC interpolation kernel  $\delta_{\Delta,\sigma}$  is used for information transfer between different subdomains. In an iterative process, the use of pseudo-overlapping zones will lead to fast global convergence. The performance of the present approach lies in the unique use of the DSC algorithm for both data interpolation and the spatial discretization of the governing equations. Since the DSC algorithm is a local approach with user-defined computational bandwidth and controllable approximation accuracy, the present approach not only provides a high local accuracy in each subdomain, but also achieves a high global accuracy. Since the calculation in each subdomain is relatively independent, it is expected that a parallel implementation of the present method can be easily realized.

### 3.2. Spatial discretization

A staggered grid system as shown in Figure 3(b) is employed in the present investigation. For each subdomain (block), the momentum equation in the horizontal direction is written at the point  $(i + \frac{1}{2}, j)$ , the momentum equation in the vertical direction is written at the point  $(i, j + \frac{1}{2})$ , and the pressure is given at point  $(i, j)$ . The continuity equation is approximated at the point  $(i, j)$ . All spatial derivatives in Equations (10) and (11) are discretized by using the DSC algorithm. A uniform grid in both  $x$ - and  $y$ -directions for each block is employed in this work. The discretized forms of Equations (6)–(9) are expressed as follows:

$$D_h(U) = \sum_{k=-W}^W \delta_{\Delta,\sigma}^{(1)}(k\Delta x_N) u_{i+k,j} + \sum_{k=-W}^W \delta_{\Delta,\sigma}^{(1)}(k\Delta y_N) v_{i,j+k} \tag{14}$$

$$\nabla_h p = \left[ \sum_{k=-W}^W \delta_{\Delta,\sigma}^{(1)}(k\Delta x_N) p_{i+k,j}, \sum_{k=-W}^W \delta_{\Delta,\sigma}^{(1)}(k\Delta y_N) p_{i,j+k} \right]^T \tag{15}$$

$$f_h = \frac{1}{Re} \left[ \sum_{k=-W}^W \delta_{\Delta, \sigma}^{(2)}(k\Delta x_N) u_{i+\frac{1}{2}+k, j} + \sum_{k=-W}^W \delta_{\Delta, \sigma}^{(2)}(k\Delta y_N) u_{i+\frac{1}{2}, j+k} \right] \\ - \left[ u_{i+\frac{1}{2}, j} \sum_{k=-W}^W \delta_{\Delta, \sigma}^{(1)}(k\Delta x_N) u_{i+\frac{1}{2}+k, j} + v_{i+\frac{1}{2}, j} \sum_{k=-W}^W \delta_{\Delta, \sigma}^{(1)}(k\Delta y_N) u_{i+\frac{1}{2}, j+k} \right] \quad (16)$$

$$g_h = \frac{1}{Re} \left[ \sum_{k=-W}^W \delta_{\Delta, \sigma}^{(2)}(k\Delta x_N) v_{i+k, j+\frac{1}{2}} + \sum_{k=-W}^W \delta_{\Delta, \sigma}^{(2)}(k\Delta y_N) v_{i, j+\frac{1}{2}+k} \right] \\ - \left[ u_{i, j+\frac{1}{2}} \sum_{k=-W}^W \delta_{\Delta, \sigma}^{(1)}(k\Delta x_N) v_{i+k, j+\frac{1}{2}} + v_{i, j+\frac{1}{2}} \sum_{k=-W}^W \delta_{\Delta, \sigma}^{(1)}(k\Delta y_N) v_{i, j+\frac{1}{2}+k} \right] \quad (17)$$

$$L_h(U) = F_h(U) - \nabla_h p$$

$$F_h(U) = [f_h, g_h]^T \quad (18)$$

where  $\delta_{\Delta, \sigma}^{(1)}$  and  $\delta_{\Delta, \sigma}^{(2)}$  are coefficients of the regularized Shannon kernel (RSK). Here,  $\Delta x_N$  and  $\Delta y_N$  denote the grid spacings in the  $x$ - and  $y$ -directions, respectively, for the  $N$ th computational block.

Note that in the expression for  $U$ , the values of both velocity components  $u$  and  $v$  are obtained at point  $(i, j)$ . It is, therefore, necessary to transfer their values into the points  $(i + \frac{1}{2}, j)$  and  $(i, j + \frac{1}{2})$ , respectively. Meanwhile, in Equations (16)–(18), the values of velocity component  $u$  need to be computed at point  $(i, j + \frac{1}{2})$ . Similarly, the values of velocity component  $v$  need to be computed at point  $(i + \frac{1}{2}, j)$ . We can use the DSC algorithm to perform these transformations and to obtain their values at the specified points as follows:

$$u_{i, j+\frac{1}{2}} = \sum_{k=-W}^W \delta_{\Delta, \sigma}^{(0)} \left( \left( k - \frac{1}{2} \right) \Delta y_N \right) u_{i, j+k} \quad (19)$$

$$u_{i+\frac{1}{2}, j} = \sum_{k=-W}^W \delta_{\Delta, \sigma}^{(0)} \left( \left( k - \frac{1}{2} \right) \Delta x_N \right) u_{i+k, j} \quad (20)$$

$$v_{i, j+\frac{1}{2}} = \sum_{k=-W}^W \delta_{\Delta, \sigma}^{(0)} \left( \left( k - \frac{1}{2} \right) \Delta y_N \right) v_{i, j+k} \quad (21)$$

$$v_{i+\frac{1}{2}, j} = \sum_{k=-W}^W \delta_{\Delta, \sigma}^{(0)} \left( \left( k - \frac{1}{2} \right) \Delta x_N \right) v_{i+k, j} \quad (22)$$

where  $\delta_{\Delta, \sigma}^{(0)}$  is the coefficient of the RSK.

By substituting Equations (14)–(18) into Equations (10) and (11), the following semi-discretized approximation for Equations (10) and (11) is obtained

$$D_h(U) = 0 \quad (23)$$

$$\frac{dU}{dt} = L_h(U) = F_h(U) - \nabla_h p \quad (24)$$

Here the subscripts  $i, j$  on the left hand side of Equation (24) are omitted for simplicity. These equations are discretized in time in the next subsection.

### 3.3. Temporal discretization and the treatment of pressure

The third-order Runge–Kutta (R–K) scheme is used for the temporal discretization. The scheme has third-order accuracy in time and was used in the literature [39, 35]. Updating the pressure field requires special care. At each step of the R–K scheme, the FTSPFM [35] is adopted to solve Equations (23) and (24). We refer the reader to Reference [35] for the detailed description of the temporal discretization and the treatment of pressure for a single domain. In the present work, intersubdomain iterations are further required.

## 4. RESULTS AND DISCUSSION

### 4.1. Accuracy assessment of the scheme

The Taylor problem is a popular benchmark with a known closed form solution. Such a problem renders a rigorous assessment on the order of accuracy of the present scheme. For the two-dimensional incompressible flow with periodic boundary conditions in both directions, the exact solution is given by

$$u(x, y, t) = -\cos(kx) \sin(ky) \exp(-2k^2t/Re) \quad (25)$$

$$v(x, y, t) = \sin(kx) \cos(ky) \exp(-2k^2t/Re) \quad (26)$$

$$p(x, y, t) = -(\cos(2kx) + \cos(2ky)) \exp(-4k^2t/Re)/4.0 \quad (27)$$

When  $t=0$ , above solution yields the initial conditions. By increasing the wave number  $k$ , one can use this problem to examine the resolution of new numerical schemes.

The incompressible Navier–Stokes equations with the Reynold's number of 1000 and three different wavenumbers  $k=2, 4$  and 8 are solved in this assessment. Different combinations of mesh size and computational bandwidth are examined. For simplicity, we adopt uniform mesh size  $1/N$  in both directions. Numerical errors are evaluated when equations are solved to  $t=2$  (see Tables I and II).

The two parameters which influence numerical order are, bandwidth and the mesh size. For  $W=8$ , the numerical order is relatively low, though the accuracy is essentially high. While the bandwidth is increased to 16, the numerical order of the scheme also improves substantially.

Table I. Numerical errors, orders and relative CPU times in solving the Taylor problem ( $t=2, k=2$ ).

$W$	$N=16$		$N=32$		Order
	$L_\infty$	CPU(s)	$L_\infty$	CPU(s)	
8	8.47E-6	7.5	8.89E-7	67.2	3.25
16	5.22E-8	12.9	7.45E-11	74.1	9.45
32	—	—	8.48E-14	147.4	—

Table II. Numerical errors, orders and relative CPU times in solving the Taylor problem with high wavenumbers ( $t=2$ ).

$k=4$					$k=8$				
$N$	$W$	$L_\infty$	CPU(s)	Order	$N$	$W$	$L_\infty$	CPU(s)	Order
16	16	3.92E-05	9.1	—	32	32	3.96E-6	71.6	—
32	16	2.24E-08	54.2	11.77	64	32	1.06E-11	546.2	18.51
32	32	9.46E-13	114.4	—			—		

A relatively long CPU time is required when the computation is set at a very high accuracy. It is noted that for cases  $N=16, k=4$  and  $N=32, k=8$ , the pressure fields are solved at the Nyquist critical sampling rate, i.e. two grid points per wavelength. Such a spectral resolution is consistent with the discrete Fourier analysis given in Figure 2 and the mathematical analysis reported in Reference [37].

#### 4.2. Further validation

**4.2.1. Single lid driven cavity.** As a precursor to the problem of double shear driven cavity, we test the present approach by studying the popular single lid driven cavity flow. The flow domain for this problem is a unit square, with an upper lid driving the flow in the cavity. The flow features are simulated at two different Reynold's numbers of 100 and 1000 for a comparison. At  $Re=100$ , a uniform grid of  $65 \times 65$  is used in the present study, which is smaller than that used by Ghia *et al.* [41] in their benchmark work. The horizontal and vertical velocity distribution along the centreline are compared in Figure 4 for both simulations. An excellent comparison can be seen. Similarly, good comparison can also be observed for velocity distributions at a higher Reynold's number,  $Re=1000$ , where both results are simulated by the grid of  $129 \times 129$ . In fact, a good quantitative agreement between the two results has been observed for many other Reynold's numbers, as well.

**4.2.2. Convergence and consistence issues.** Establishing convergence and consistence forms a fundamental step for any numerical simulation. This in turn, requires a careful and systematic investigation. Thus, the objective of this subsection is to pursue these issues and to establish confidence for using the DSC algorithm. For a problem like the staggered double shear driven cavity, error assessment is a key issue as the analytical solution is not available. The real size of error can never be computed. Nevertheless, it is possible to construct an estimate of such an error. Error in a strict sense, may be defined as the difference between exact and approximate solutions. A variety of estimated error norms are available. In the present study, reduction in incremental error between two successive iterations was taken as the criterion for convergence. Error is defined as

$$E_{in}^n = \max |\eta^{n+1} - \eta^n| \quad (28)$$

where,  $\eta$  refers to the primitive variable of interest, such as the velocity or pressure. The variation of  $E_{in}^n$  against time can be regarded as the temporal history of convergence and a typical plot is given in Figure 5, for  $Re=100$  and 1000. To ensure a steady state solution, the following inequality,  $E_{in}^n \leq 10^{-7}$ , is satisfied in all simulations.

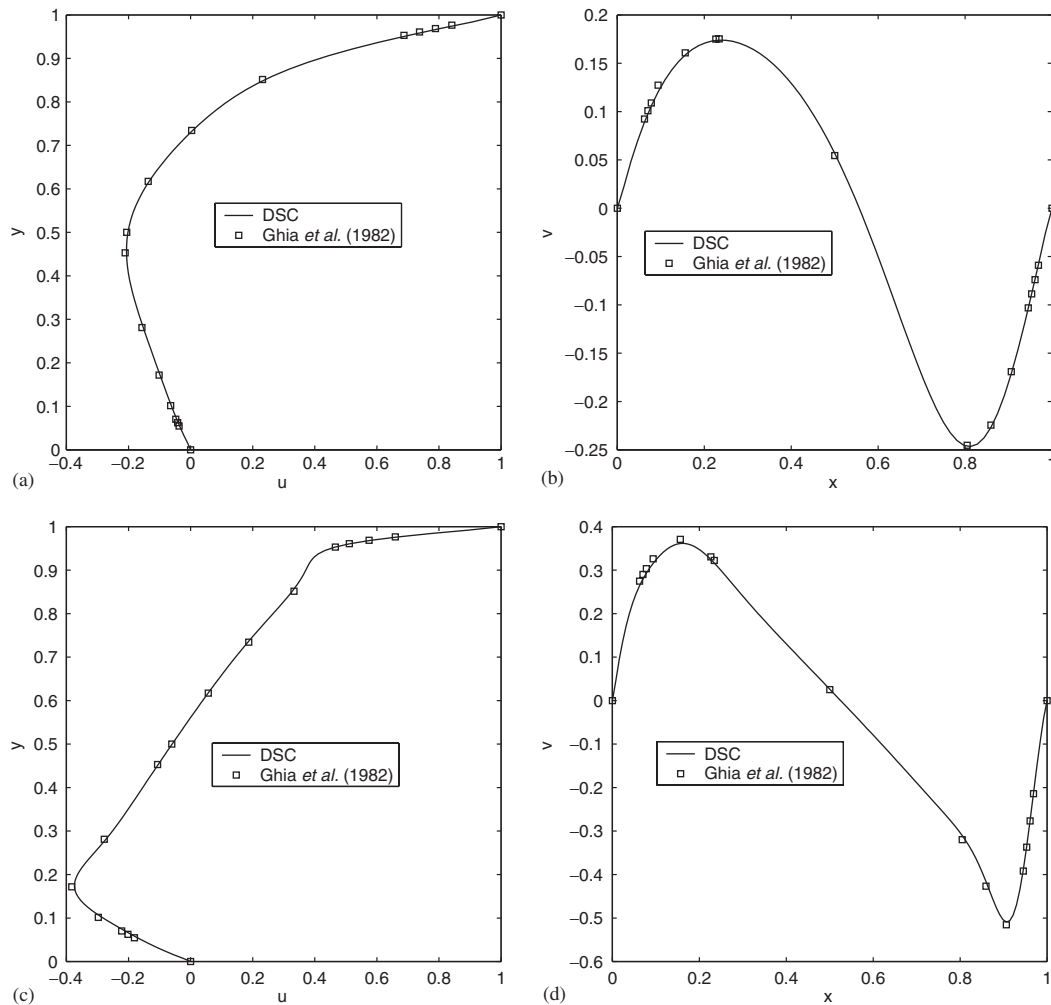


Figure 4. Comparison of velocities for a single lid driven cavity. Horizontal velocity along mid width: (a)  $Re = 100$ ; (c)  $Re = 1000$ . Vertical velocity along mid height: (b)  $Re = 100$ ; (d)  $Re = 1000$ .

A demonstration of the temporal convergence alone is not sufficient for ensuring the correctness of the solution. Furthermore, it is required to prove that, the algebraic equations being solved are consistent with the physical model. Therefore, errors due to truncation, round off, approximations, interpolation, etc., which might have accumulated during the course of numerical discretization cannot be allowed to be magnified, and hence, need to be minimized. This objective can be achieved by arriving at a reliable and a grid independent mesh, by systematic grid refinement. As mentioned earlier, the computational domain under investigation is divided into five subdomains (see Figure 1). Four pseudooverlapping grids (POGs) are employed in the present investigation as shown in Table III. In Tables IV and V, horizontal and vertical velocities are summarized, respectively, for the flow at  $Re = 1000$ . As can be observed, owing

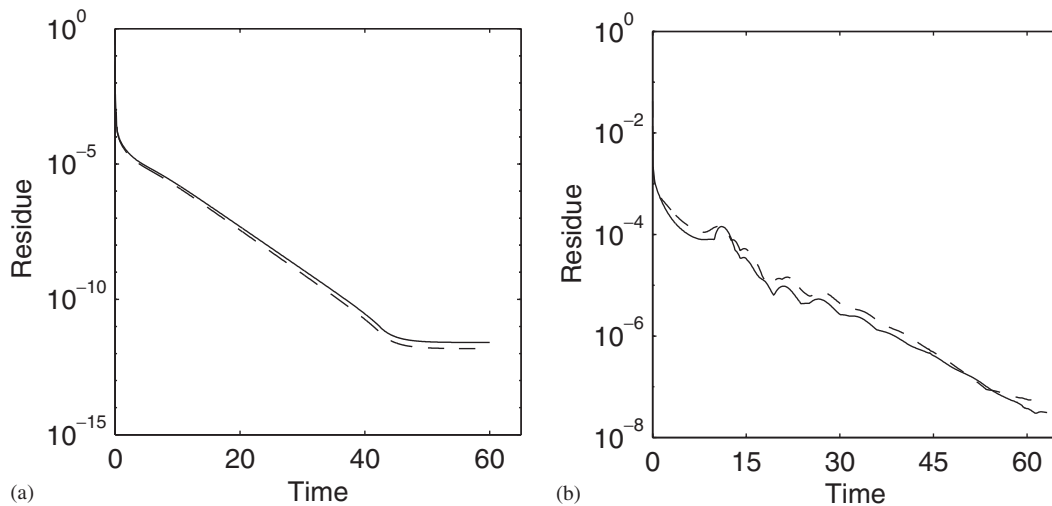


Figure 5. Temporal history of the residue for (a)  $Re = 100$ ; and (b)  $Re = 1000$ . - -  $u$ -velocity; —  $v$ -velocity.

Table III. Grid sizes employed in the pseudo-overlapping grids (POGs) in each subdomain.

Case No.	Mesh in each subdomain				
	Subdomain 1	Subdomain 2	Subdomain 3	Subdomain 4	Subdomain 5
POG I	$33 \times 33$	$33 \times 33$	$33 \times 33$	$33 \times 33$	$33 \times 33$
POG II	$129 \times 65$	$65 \times 65$	$65 \times 65$	$129 \times 65$	$65 \times 65$
POG III	$201 \times 81$	$81 \times 121$	$121 \times 121$	$201 \times 81$	$81 \times 121$
POG IV	$261 \times 105$	$105 \times 157$	$157 \times 157$	$261 \times 105$	$105 \times 157$

to the nature of high accuracy in the DSC approach, even the grid of POG-II can produce a reasonable result which compares well with those of other refined grids. Obviously, the grid of POG-III is completely adequate for the simulations by the DSC, to ensure the grid independent nature of the present investigations.

### 4.3. Velocity distribution

In the previous section we have presented some consistence studies. However, a comparison with some other available experimental and/or numerical simulations is also necessary to enhance the reliability of the simulations. Unfortunately, no quantitative data are available in the open literature for such a comparison exercise. Therefore, we have made use of a standard finite volume based approach for the numerical simulation of mass and momentum conservation equations using the SIMPLE scheme of Patankar [18]. The basic steps involved in the second order accurate finite volume based scheme are as follows: (i) solve the momentum equations, (ii) solve the pressure correction equations, and (iii) check for iterative convergence. For reasons of brevity, no further details about this well documented approach are discussed.

Table IV. Grid sensitivity studies for horizontal velocity ( $u$ ) along mid width ( $x = 0.7$ ) for  $Re = 1000$ . POG: pseudo-overlapping grid.

$y$ -co-ordinate	POG I	POG II	POG III	POG IV
0.0	-1.0000	-1.0000	-1.0000	-1.0000
0.1	0.1434	0.1541	0.1565	0.1567
0.2	-0.0848	-0.0925	-0.0970	-0.1013
0.3	-0.2774	-0.2971	-0.3054	-0.3104
0.4	-0.2766	-0.2915	-0.2962	-0.2984
0.5	-0.1888	-0.1972	-0.2013	-0.2018
0.6	-0.0950	-0.0992	-0.1026	-0.1020
0.7	-0.0003	-0.0006	-0.0021	-0.0014
0.8	0.0944	0.0979	0.0981	0.0990
0.9	0.1877	0.1953	0.1959	0.1982
1.0	0.2746	0.2888	0.2889	0.2935
1.1	0.2772	0.2974	0.3058	0.3107
1.2	0.0866	0.0962	0.1074	0.1082
1.3	-0.1414	-0.1505	-0.1460	-0.1497
1.4	1.0000	1.0000	1.0000	1.0000

Table V. Grid sensitivity studies for vertical velocity ( $v$ ) along mid height ( $y = 0.7$ ) for  $Re = 1000$ . POG: pseudo-overlapping grid.

$x$ -co-ordinate	POG I	POG II	POG III	POG IV
0.0	0.0000	0.0000	0.0000	0.0000
0.1	0.2303	0.2494	0.2564	0.2609
0.2	0.2708	0.2842	0.2872	0.2911
0.3	0.1834	0.1914	0.1953	0.1979
0.4	0.1308	0.1366	0.1408	0.1417
0.5	0.0851	0.0891	0.0925	0.0924
0.6	0.0427	0.0445	0.0464	0.0461
0.7	0.0003	0.0003	0.0002	0.0001
0.8	-0.0422	-0.0440	-0.0460	-0.0459
0.9	-0.0846	-0.0886	-0.0921	-0.0922
1.0	-0.1299	-0.1362	-0.1405	-0.1416
1.1	-0.1836	-0.1915	-0.1957	-0.1981
1.2	-0.2715	-0.2849	-0.2890	-0.2922
1.3	-0.2314	-0.2495	-0.2558	-0.2605
1.4	0.0000	0.0000	0.0000	0.0000

The plots of both horizontal and vertical velocities along the mid section of the cavity are plotted in Figure 6. The central sections (mid height and mid width) are chosen, as they represent maximum variation for the horizontal and vertical velocity profiles. There is a good agreement between the results of the DSC and those of the standard finite volume based approach.

Figure 7 depicts the velocity distribution for different Reynold's numbers ( $Re = 50, 100, 400, 1000$ ). The horizontal velocity profile has a slower variation in the core region and a larger gradient closer to the moving lids. With increase in Reynold's number, the dominance of the inertial forces can be noticed, which leads to a larger gradient close to the walls and

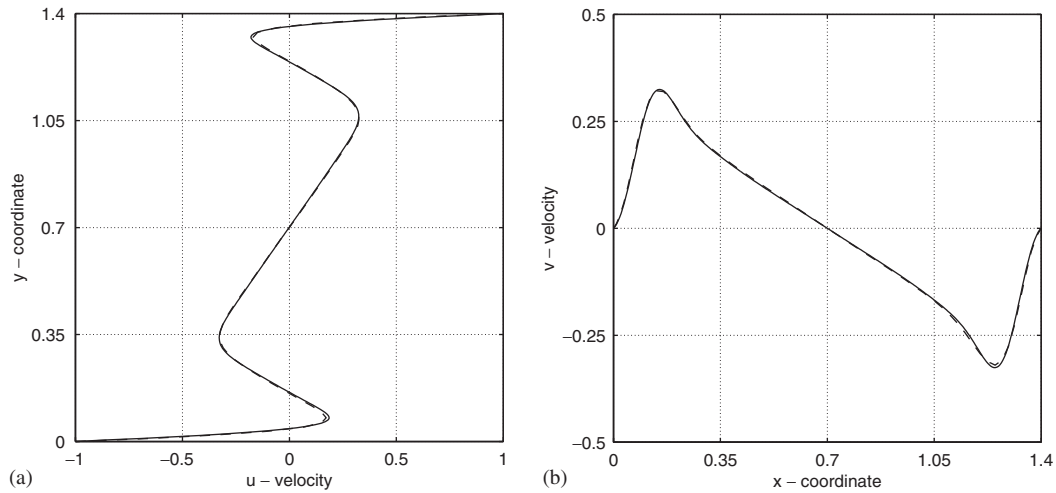


Figure 6. Validation of results with a finite volume based approach for  $Re = 1000$ . - - Finite volume method; — DSC: (a) horizontal velocity at mid width ( $x = 0.7$ ); and (b) vertical velocity at mid height ( $y = 0.7$ ).

a criss-cross variation in the core region. The horizontal velocity gradient is larger in a zone closer to the lid walls. The location of vertical velocity peaks move towards the left and right edges with the increase in Reynold's number, indicating the dominance of a stronger recirculatory eddy. Quantitatively, both horizontal and vertical velocities are listed in Tables VI and VII for different Reynold's numbers. These results may serve as benchmarks for further work.

#### 4.4. Fluid flow patterns

The prevalence of rich and complex fluid flow patterns in a staggered double shear driven cavity further vindicates the choice of this problem for investigation. Initially, the cavity is filled with the fluid and is assumed to be quiescent. Then, a clock-wise momentum is imparted to the fluid, by the two driving lids on the top and bottom, when they are set into an anti-parallel wall motion. The upper lid moves to the right, while the lower one to the left, both with the same speed. Thus, this problem essentially translates as an extension to the popularly known lid driven square cavity problem. The Reynold's number is the single most influential parameter of interest, representing both inertial and viscous forces in the simulation. Its value is varied in the range of 50–1000. This range is carefully chosen, such that, it falls well with in the assumptions of two-dimensionality and laminar flow. Recently, in connection with the single lid driven cavity, the lack of steadiness and incipience of three dimensionality were reported beyond a Reynold's number of 7500. However, such a value is not available for the staggered double shear driven cavity as it should have to be established from a thorough comparison of both two and three-dimensional simulations. Therefore, in the present investigation, we confine to a very safe range of values which are much smaller than 7500.

Figure 8 depicts the velocity vectors, streamlines and both  $u$  and  $v$  velocity contours, over a range of Reynold's numbers (from 50 to 1000). These plots are essentially four different forms of fluid flow representation. These features can be grossly classified into two

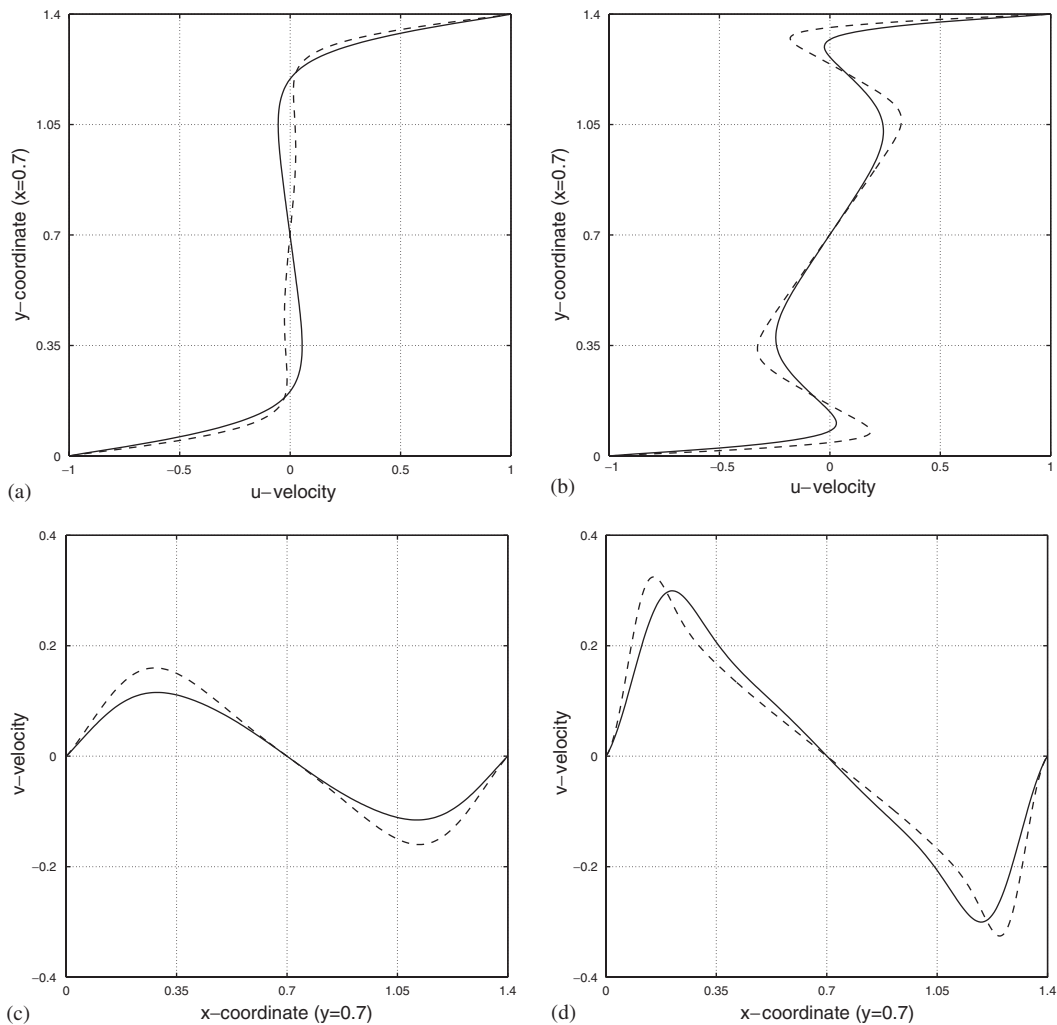


Figure 7. Variation of horizontal ( $u$ ) velocity along mid width ( $x=0.7$ ): (a) —  $Re=50$ ; - -  $Re=100$ ; (b) —  $Re=400$ ; - -  $Re=1000$ ; Variation of vertical ( $v$ ) velocity along mid height ( $y=0.7$ ): (c) —  $Re=50$ ; - -  $Re=100$ ; and (d) —  $Re=400$ ; - -  $Re=1000$ .

categories: two primary eddy pattern and a merged primary vortex pattern. At low Reynold's numbers ( $Re=50, 100$ ), twin primary eddies are formed between the two driving lids. At high Reynold's numbers ( $Re=400, 1000$ ), the morphology of the flow patterns is very different. A distinct merged flow pattern is formed. Here, the two eddy centres coalesce into one primary circulation, where the fluid is accelerated by both the moving walls. The centre of this main circulation is located very close to the centre of the principal diagonal of the cavity. The formation of four secondary eddies at the corners is an interesting aspect, which essentially emulates the behaviour of the single lid driven cavity. These corner eddies grow in size with increased dominance of the inertial effects, over the viscous ones.

Table VI. Effect of Reynold's number on the horizontal velocity ( $u$ ) along mid width ( $x = 0.7$ ).

$y$ -co-ordinate	$Re = 50$	$Re = 100$	$Re = 400$	$Re = 1000$
0.0	-1.00000	-1.00000	-0.99999	-1.00000
0.1	-0.26949	-0.18422	0.02913	0.15663
0.2	-0.00517	-0.01944	-0.08917	-0.09860
0.3	0.05070	-0.01732	-0.21418	-0.30739
0.4	0.05161	-0.02498	-0.24160	-0.29724
0.5	0.03710	-0.02378	-0.18515	-0.20144
0.6	0.01873	-0.01391	-0.09627	-0.10195
0.7	-0.00058	-0.00072	-0.00109	-0.00162
0.8	-0.01977	0.01261	0.09376	0.09851
0.9	-0.03775	0.02289	0.18191	0.19726
1.0	-0.05160	0.02484	0.23861	0.29169
1.1	-0.05008	0.01800	0.21456	0.30773
1.2	0.00595	0.02053	0.09325	0.10635
1.3	0.26999	0.18505	-0.02458	-0.14875
1.4	1.00000	1.00000	1.32500	1.00000

Table VII. Effect of Reynold's number on the vertical velocity ( $v$ ) along mid height ( $y = 0.7$ ).

$x$ -co-ordinate	$Re = 50$	$Re = 100$	$Re = 400$	$Re = 1000$
0.0	0.00000	0.00000	0.00000	0.00000
0.1	0.06080	0.07841	0.17319	0.25745
0.2	0.10392	0.14301	0.29856	0.28866
0.3	0.11530	0.15908	0.24824	0.19675
0.4	0.10223	0.13354	0.17056	0.14115
0.5	0.07560	0.08964	0.11343	0.09208
0.6	0.04024	0.04321	0.05895	0.04595
0.7	-0.00004	0.00007	0.00052	0.00011
0.8	-0.04025	-0.04307	-0.05792	-0.04571
0.9	-0.07549	-0.08948	-0.11262	-0.09185
1.0	-0.10209	-0.13345	-0.17040	-0.14100
1.1	-0.11528	-0.15915	-0.24881	-0.19698
1.2	-0.10400	-0.14317	-0.29932	-0.28998
1.3	-0.06088	-0.07850	-0.17328	-0.25697
1.4	0.00000	0.00000	0.00000	0.00000

The magnitude of the velocity of fluid particles which cannot be directly perceived from the streamline plots can be assessed in the velocity vectors. Two out of the four secondary eddies formed at the corners B and F are much weaker, while the other two eddies near the walls CD and GH are much stronger, which can be perceived in the form of a very small magnitude of velocity for the former. Both the  $u$  and  $v$  velocity contours are also plotted and they depict a perfect anti-symmetric pattern. The vorticity values and locations of the centres of primary and secondary vortices are listed for different Reynold's numbers in Table VIII.

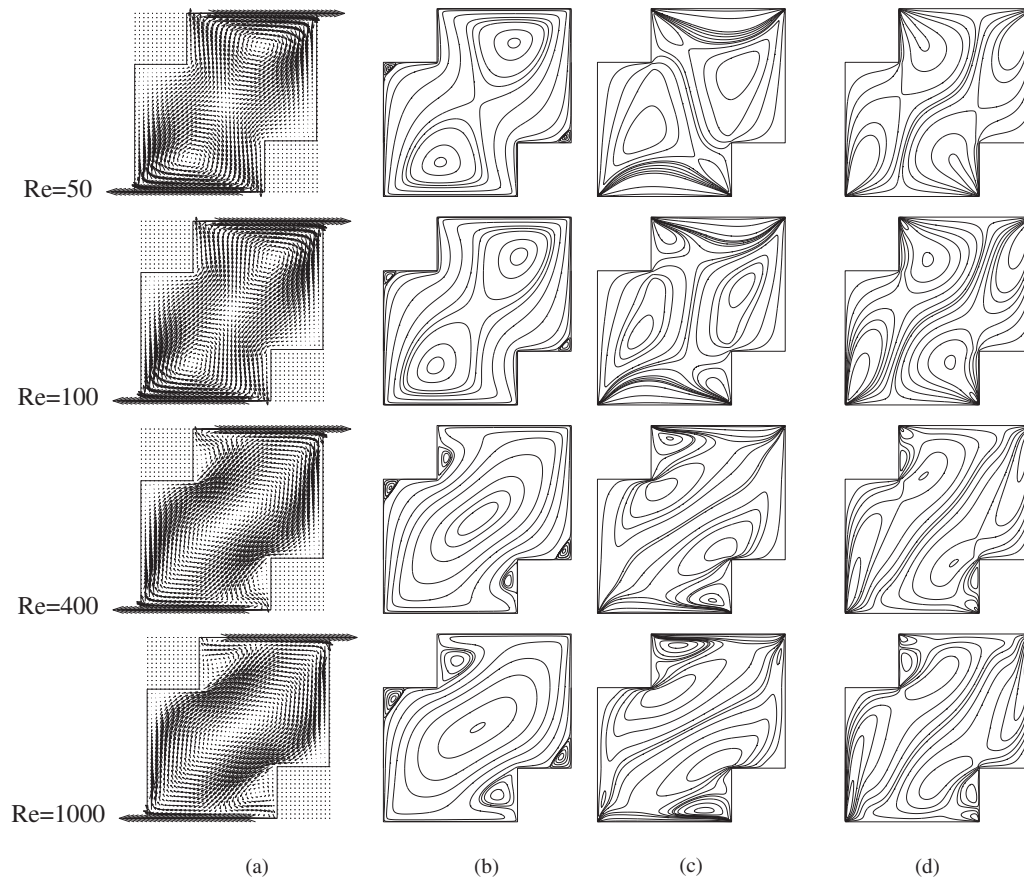


Figure 8. Fluid flow patterns at steady state for  $Re = 50, 100, 400$  and  $1000$ : (a) velocity vectors; (b) streamlines; (c)  $u$ -velocity contours; and (d)  $v$ -velocity contours.

The increase in strength of the secondary vortices can be noticed with increase in Reynold's number. These values could be useful for comparison in the future.

The vorticity contours are depicted in Figure 9. The negative vorticity is indicated by dotted lines, while the positive values by solid lines. The zones of positive vorticity are confined closer to the wall, indicating a high shear gradient, while the core region is dominated by negative vorticity. Owing to the recirculation of the secondary eddies, small negative vorticity zones are formed near the walls CD and GH at high Reynold's numbers. Positive vorticity is generated more closer to the walls with increase in the Reynold's number. Smooth pressure contours are depicted in Figure 10, which have symmetric patterns in compliance with the moving lids on the top and bottom of the cavity.

In all the simulations conducted at Reynold's numbers up to  $1000$ , perfectly symmetric patterns could be achieved due to the imposed moving boundary on both the top and bottom lids. However, it was very difficult to maintain symmetry beyond certain Reynold's number. A low accuracy numerical scheme can easily induce symmetry breaking even at a much

Table VIII. The vorticity values and corresponding locations of the centres of primary and secondary vortices.

$Re$	Primary vortex		First secondary vortex		Second secondary vortex	
	$(x, y)$	$\omega(x, y)$	$(x, y)$	$\omega(x, y)$	$(x, y)$	$\omega(x, y)$
50	(0.9781, 1.1600)	-3.05843	(1.3556, 0.4405)	0.02395		
	(0.4219, 0.2518)	-3.05670	(0.0444, 0.9595)	0.02394		
100	(1.0172, 1.1091)	-2.72390	(1.3556, 0.4486)	0.04399		
	(0.3828, 0.2889)	-2.72310	(0.0444, 0.9514)	0.04401		
400	(0.7000, 0.7000)	-1.54842	(1.3500, 0.4656)	0.15569	(0.4703, 1.1625)	1.38495
			(0.0500, 0.9344)	0.15777	(0.9219, 0.2375)	1.38140
1000	(0.7000, 0.7000)	-1.41562	(1.3250, 0.4844)	0.53846	(0.5484, 1.2000)	2.38557
			(0.0750, 0.9063)	0.53813	(0.7256, 0.2000)	2.38559

lower value of Reynold's number. What makes the present simulation very challenging is the fact that this system admits elliptic instability. It takes a great deal of effort to distinguish a numerically induced asymmetric flow pattern from that created by the elliptic instability, which likes the Kármán vortex shedding behind the flow past a circular cylinder, is a part of the flow instability. In this regard, the DSC algorithm is extremely helpful. It gives us confidence to study the symmetry aspect, as it inherently possesses the advantage of controllable accuracy in one setting. It would be of interest to study how a change in the order of accuracy could induce asymmetry into the system. Figure 11 depicts two flow patterns obtained at  $Re = 3200$ . The flow essentially remains symmetric, for a very long time before it finally switches to an asymmetric morphology. Such a change is irreversible, as a typical fingerprint of the elliptic instability. Further investigations are under progress in this direction.

## 5. CONCLUSION

The problem of staggered double shear driven cavity is introduced in the context of benchmarking, for new computational schemes. It is believed that this problem has the potential to become as popular as the other benchmark problems, like the square driven cavity, backward facing step, flow past a circular cylinder, etc. Most existing test problems are somewhat unidirectional. Through the present problem, one can examine a variety of fluid flow features, including symmetry, numerically induced symmetry breaking, and elliptic instability, which is not possible to verify from most other existing benchmark problems. The wavelet based discrete singular convolution (DSC) is proposed for the spatial discretization. The philosophy underpinning the DSC algorithm is discussed. A fractional time step potential function method (FTSPFM) is employed for the numerical implementation of the Navier–Stokes equations. The successive over relaxation (SOR) scheme is used for solving the Poisson equation, which was formulated for the potential function. A third order Runge–Kutta scheme is used for the time integration. The DSC algorithm is validated by solving the Taylor problem and by a comparison with the benchmark solution by Ghia *et al.* [41] for the single lid driven cavity flow. A popular finite volume based scheme is employed to further validate our results

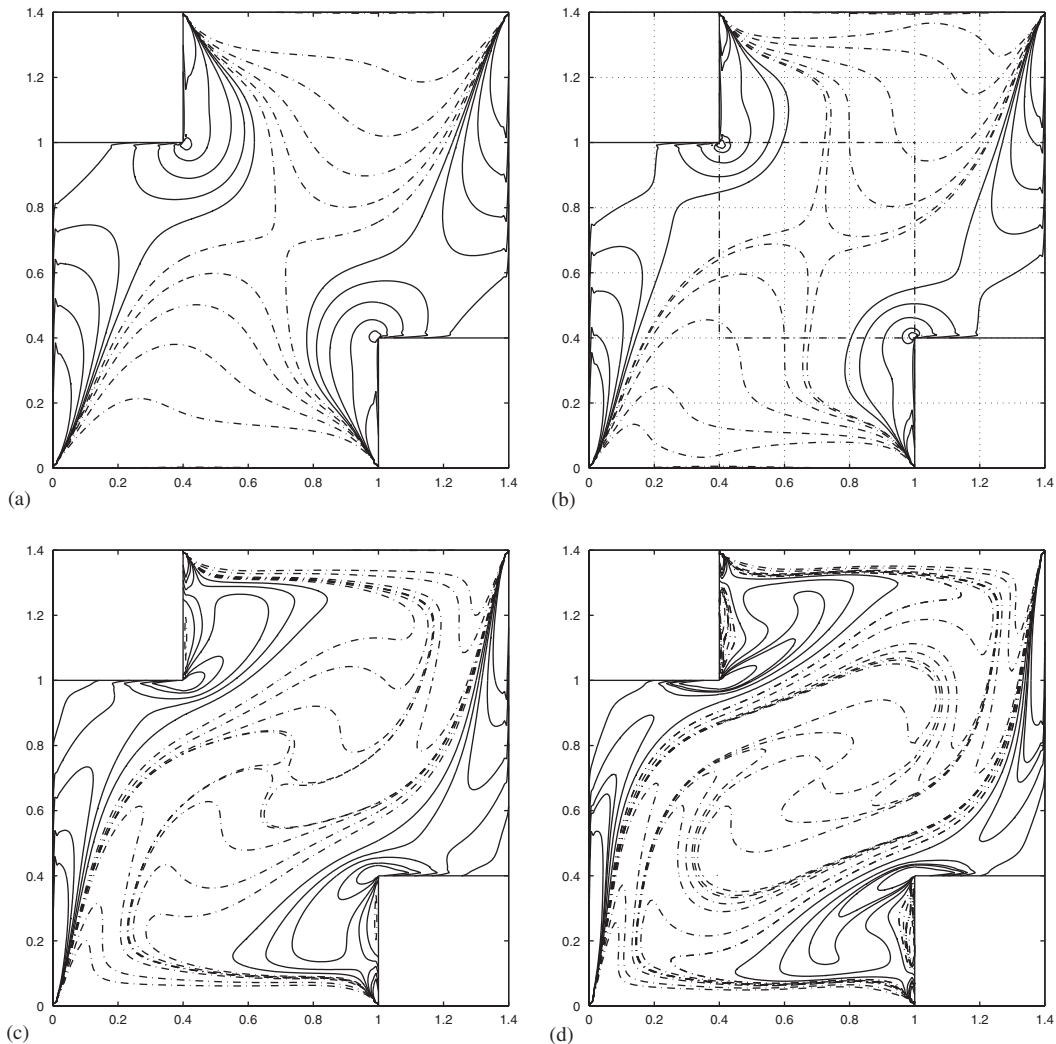


Figure 9. Vorticity contours for different Reynold's numbers: (a)  $Re = 50$ ; (b)  $Re = 100$ ; (c)  $Re = 400$ ; and (d)  $Re = 1000$ .

on the staggered double lid driven cavity flow. Some remarks can be outlined as follows:

- The wavelet-based DSC algorithm provides high accuracy spatial discretizations. One of the major attractive features of the present DSC approach is its controllable accuracy which is attained by an appropriate choice of the DSC parameter  $W$ , as verified with the Taylor problem.
- Pseudo-overlapping subdomains are used to divide the computational domain into smaller regions. An equi-spaced stencil is employed in each subdomain. Equipped with this domain decomposition approach, the high accuracy DSC algorithm can also be used to

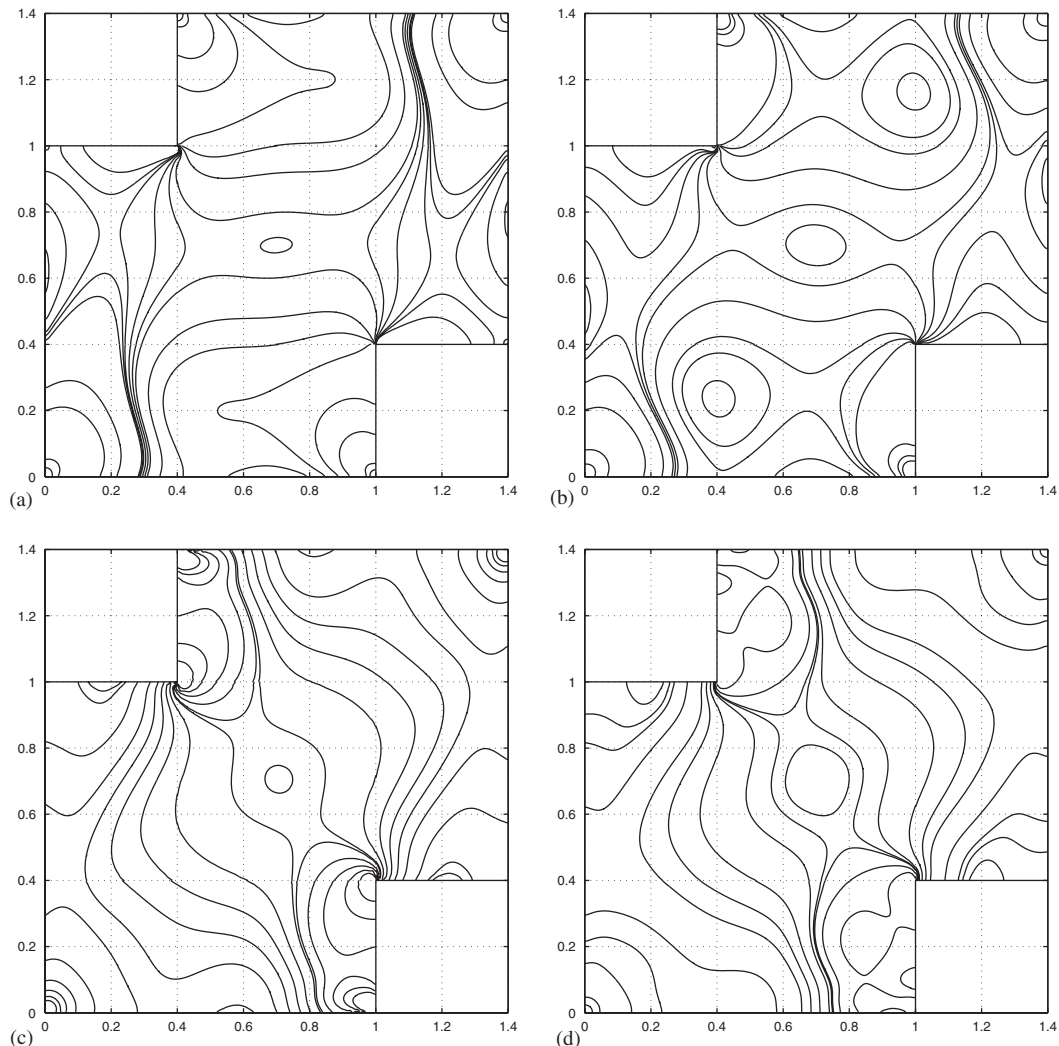


Figure 10. Pressure contours for different Reynold's numbers: (a)  $Re = 50$ ; (b)  $Re = 100$ ; (c)  $Re = 400$ ; and (d)  $Re = 1000$ .

treat flow problem with complex geometry and the overall method also has the potential to be used in parallel architecture.

- The present DSC algorithm is tested by computing the single lid driven cavity flow for which benchmark solution is available. Results on the staggered double lid driven cavity flow are validated by extensive studies on consistence and convergence to achieve reliability. A standard second order finite volume scheme is employed for cross-validation of the proposed approach.
- For the double lid driven cavity, benchmark quality solution is obtained over a range of Reynold's numbers. Qualitative fluid flow features such as, streamlines, velocity,

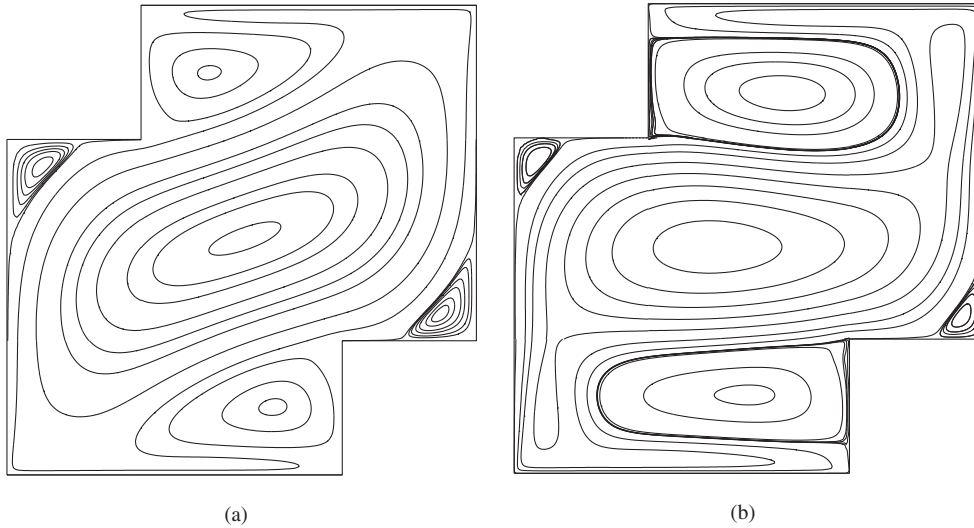


Figure 11. The existence of: (a) symmetric and (b) asymmetric patterns at  $Re = 3200$ . The latter pattern was obtained after a long-time integration and is attributed to the mechanism of elliptic instability.

pressure and vorticity contours are depicted. Quantitative results of velocity values are tabulated.

- Flow pattern topology of two distinct features is observed. Two primary vortex type flow pattern was found at low Reynold's numbers and a single merged primary vortex patterns occur at high Reynold's numbers.
- The secondary eddies are observed at four corners. Their strength increases with the increase in Reynold's number.
- The high accuracy of the present scheme enables as a check on the issue of symmetry. The elliptic instability can be distinguished from numerically induced asymmetric patterns. Symmetric solution is obtained for Reynold's number below 1000, whereas elliptic instability occurs at  $Re = 3200$ , in which both asymmetric and symmetric flow patterns are observed.

#### ACKNOWLEDGEMENTS

This work was supported by the National University of Singapore and the National Science and Technology Board of the Republic of Singapore.

#### REFERENCES

1. Shankar PN, Deshpande MD. Fluid mechanics of the driven cavity. *Annual Review of Fluid Mechanics* 2000; **32**:93–136.
2. Albensoeder S, Kuhlmann HC, Rath HJ. Multiplicity of steady two-dimensional flow in two-sided lid driven cavities. *Theoretical and Computational Fluid Dynamics* 2001; **14**:223–241.
3. Kuhlmann HC, Wanschura M, Rath HJ. Flow in two-sided lid driven cavities: non-uniqueness, instabilities, and cellular structures. *Journal of Fluid Mechanics* 1997; **336**:267–299.
4. Hinatsu M, Ferziger JH. Numerical computation of unsteady incompressible flow in complex geometry using a composite multigrid technique. *International Journal for Numerical Methods in Fluids* 1991; **13**:971–997.
5. Gottlieb D, Hussaini MY, Orszag SA. In *Spectral Methods for Partial Differential Equations*, Voigt RG, Gottlieb D, Hussaini MY (eds). SIAM: Philadelphia, 1984.

6. Canuto C, Hussaini MY, Quarteroni A, Zang TA. *Spectral Methods in Fluid Dynamics*. Springer-Verlag: Berlin, 1988.
7. Fornberg B. *A Practical Guide to Pseudospectral Methods*. Cambridge University Press, 1996.
8. Cooley JW, Tukey JW. An algorithm for the machine calculation of complex Fourier series. *Mathematics of Computation* 1965; **19**:297–301.
9. Walker JS. *Fast Fourier Transforms*. CRC Press: Florida, 1996.
10. Bellman R, Kashef BG, Casti J. A technique for the rapid solution of nonlinear partial differential equations. *Journal of Computational Physics* 1972; **10**:40–52.
11. Forsythe GE, Wasow WR. *Finite-difference Methods for Partial Differential Equations*. Wiley: New York, 1960.
12. Tsai WT, Yue DKP. Computation of nonlinear free-surface flows. *Annual Review of Fluid Mechanics* 1996; **28**:249.
13. Zienkiewicz OC. *The Finite Element Method in Engineering Science*. McGraw-Hill: London, 1971.
14. Lewis RW, Morgan K, Thomas HR, Seetharamu KN. *The Finite Element Method in Heat Transfer*. Wiley: New York, 1994.
15. Reddy JN. *Energy and Variational Methods in Applied Mechanics*. Wiley: New York, 1984.
16. Glowinski R, Pironneau O. Finite element methods for Navier–Stokes equations. *Annual Review of Fluid Mechanics* 1992; **24**:167–204.
17. Cheung YK. *Finite Strip Methods in Structural Analysis*. Pergamon Press: Oxford, 1976.
18. Patankar SV. *Numerical Heat Transfer and Fluid Flow*. McGraw-Hill: New York, 1980.
19. Agouzal A, Debit N. Space-time domain decomposition methods for scalar conservation law. *Communications in Numerical Methods in Engineering* 1997; **13**:777–783.
20. Keskar J, Lyn DA. Computations of a laminar backward-facing step flow at  $Re = 800$  with a spectral domain decomposition method. *International Journal for Numerical Methods in Fluids* 1999; **29**:411–427.
21. Wei GW. Discrete singular convolution for the solution of the Fokker–Planck equations. *Journal of Chemical Physics* 1999; **110**:8930–8942.
22. Wei GW. A unified approach for solving the Fokker–Planck equation. *Journal of Physics A* 2000; **33**:343–352.
23. Wei GW. Wavelet generated by using discrete singular convolution kernels. *Journal of Physics A* 2000; **33**:8577–8596.
24. Wei GW. Solving quantum eigenvalue problems by discrete singular convolution. *Journal of Physics B* 2000; **33**:343–352.
25. Wei GW. A unified method for solving Maxwell’s equation. In *Proceedings of the 1999 Asia-Pacific Microwave Conference*, Singapore, 30 November, 1999; 562–565.
26. Wei GW. A new algorithm for solving some mechanical problems. *Computer Methods in Applied Mechanics and Engineering* 2001; **190**:2017–2030.
27. Wei GW. Vibration analysis by discrete singular convolution. *Journal of Sound and Vibration* 2001; 535–553.
28. Wei GW. Discrete singular convolution for beam analysis. *Engineering Structures* 2001; 1045–1053.
29. Wei GW. Synchronization of single-side locally averaged adaptive coupling and its application to shock capturing. *Physical Review Letters* 2001; **86**:3542–3545.
30. Wei GW. Discrete singular convolution method for the Sine-Gordon equation. *Physica D* 2000; **137**:247–259.
31. Ablowitz MJ, Herbst BM, Schober C. On numerical solution of the Sine-Gordon equation. *Journal of Computational Physics* 1996; **126**:299–314.
32. Guan S, Lai C.-H., Wei GW. Bessel-Fourier analysis of patterns in a circular domain. *Physica D* 2001; **151**:83–98.
33. Wei GW, Zhao YB, Xiang Y. Discrete singular convolution and its application to the analysis of plates with internal supports. I Theory and algorithm. *International Journal for Numerical Methods in Engineering* 2002; **55**:913–946.
34. Xiang Y, Zhao YB, Wei GW. Discrete singular convolution and its application to the analysis of plates with internal supports. II Complex supports. *International Journal for Numerical Methods in Engineering* 2002; **55**:947–971.
35. Wan DC, Zhou YC, Wei GW. Numerical solution of unsteady incompressible flows by the discrete singular convolution. *International Journal for Numerical Methods in Fluids* 2002; **38**:789–810.
36. Wan DC, Patnaik BSV, Wei GW. A new benchmark quality solution for the buoyancy driven cavity by discrete singular convolution. *Numerical Heat Transfer: Part B. Fundamentals* 2001; **40**:199–228.
37. Bao G, Wei GW, Zhou AH. Analysis of regularized Whittaker-Kotel’nikov-Shannon sampling expansion. *SIAM Journal on Numerical Analysis*, submitted.
38. Chorin AJ. Numerical simulation of Navier–Stokes equations. *Mathematics of Computation* 1968; **22**:745–762.
39. Shu C.-W, Osher S. Efficient implementation of essentially non-oscillatory shock-capturing schemes. *Journal of Computational Physics* 1988; **77**:439–471.
40. Peyret R, Taylor TD. *Computational Methods for Fluid Flow*. Springer Ser. Comput Phys., Springer: Berlin, Heidelberg, 1980.
41. Ghia U, Ghia KN, Shin CT. High-Resolutions for incompressible flow using the Navier–Stokes equations and a multigrid method. *Journal of Computational Physics* 1982; **48**:387–411.